Author/s:
Wang, HY;Ge, JY;Hua, C;Jiao, CQ;Wu, Y;Leong, CF;D'Alessandro, DM;Liu, T;Zuo, JL

Title:
Photo- and Electronically Switchable Spin-Crossover Iron(II) Metal–Organic Frameworks Based on a Tetrathiafulvalene Ligand

Date:
2017-05-08

Citation:
Wang, H. Y., Ge, J. Y., Hua, C., Jiao, C. Q., Wu, Y., Leong, C. F., D'Alessandro, D. M., Liu, T. & Zuo, J. L. (2017). Photo- and Electronically Switchable Spin-Crossover Iron(II) Metal–Organic Frameworks Based on a Tetrathiafulvalene Ligand. Angewandte Chemie International Edition, 56 (20), pp.5465-5470. https://doi.org/10.1002/anie.201611824.

Persistent Link:
https://hdl.handle.net/11343/292765

Title: Photo- and Electronically-Switchable Spin Crossover Iron(II) Metal-Organic Frameworks Based on a Tetrathiafulvalene Ligand

Authors: Hai-Ying Wang, Dr.; Jing-Yuan Ge; Carol Hua; Cheng-Qi Jiao; Yue Wu; Chanel F. Leong; Deanna M. D'Alessandro, Dr.; Tao Liu, Dr.; Jing-Lin Zuo, Dr.

To be cited as: 10.1002/anie.201611824

Link to VoR: https://doi.org/10.1002/anie.201611824

Photo- and Electronically-Switchable Spin Crossover Iron(II) Metal-Organic Frameworks Based on a Tetrathiafulvalene Ligand **

Hai-Ying Wang,[a] Jing-Yuan Ge,[a] Carol Hua,[b] Cheng-Qi Jiao,[c] Yue Wu,[a] Chanel F. Leong, [b] Deanna M. D'Alessandro,[b] Tao Liu,[c] and Jing-Lin Zuo *[a]

Abstract: *A major challenge is the development of multifunctional metal-organic frameworks (MOFs), wherein magnetic and electronic functionality can be controlled simultaneously for breakthroughs in material science. Herein, we rationally construct two three-dimensional MOFs by introducing the redox active ligand tetra(4-pyridyl)-tetrathiafulvalene (TTF(py)$_4$) and spin-crossover Fe(II) centers. The materials exhibit redox activity, in addition to thermally- and photo-induced spin-crossover. A crystal-to-crystal transformation induced by I_2 doping has also been observed and the resulting intercalated structure determined. The conductivity could be significantly enhanced (up to 3 orders of magnitude) by modulating the electronic state of the framework via oxidative doping; spin-crossover behavior was also modified and the photo-magnetic behavior was switched off. This work provides a powerful new strategy to tune the spin state and conductivity of framework materials through guest induced redox-state switching.*

In recent years, the design and study of multifunctional metal−organic frameworks (MOFs) exhibiting multiple accessible properties has attracted enormous attention owing to their potential applications across a plethora of areas such as sensing, solar energy harvesting and energy storage. Meanwhile, the exquisite control that can be achieved over the design of MOFs via rational structural modifications to the component metal ions and ligands provide unique prospects for regulating their topologies and elucidating fundamental structure−function relationships. A wide variety of metal centers have been used to synthesize multifunctional MOFs under different synthetic conditions, giving rise to unprecedented structural diversity which has been tailored for specific applications.[1] Special efforts have been focused, in particular, on new families of functional Fe(II) and Co(II)-supported frameworks.[2] The reversible conversion between low-spin (LS) and high-spin (HS) states in these materials can give rise to the spin-crossover (SCO) phenomenon, which has exceptional potential in technological applications such as data storage and display devices.[2a,3] It remains a challenge to control the SCO behavior and introduce conductivity via tuning the electronic state.

Tetrathiafulvalene (TTF, $C_6H_4S_4$), a sulfur rich conjugated core with two reversible, easily accessible oxidation states, can act as an effective linker to construct novel functional materials.[4] Recently, several coordination polymers based on the tetra(4-pyridyl)-tetrathiafulvalene (TTF(py)$_4$, Figure 1a) have been studied.[5] Some of these compounds retained the redox activity of the TTF moiety.

Inspired by the potential to obtain novel multifunctional materials with redox-switchable and multi-stimuli responsive properties, we exploit here the TTF(py)$_4$ ligand for the construction of two new Fe(II)-based MOFs, namely $\{[Fe(dca)_2][TTF(py)_4]_{0.5}\cdot 0.5CH_2Cl_2\}_n$ (**1**), $\{[Fe(dca)][TTF(py)_4]\cdot ClO_4\cdot CH_2Cl_2\cdot 2CH_3OH]\}_n$ (**2**), and the I_2-doped analogue of **2** $\{[Fe(dca)][TTF(py)_4]\cdot 0.5I_3\cdot ClO_4\cdot CH_2Cl_2\cdot CH_3OH\cdot C_6H_{12}\}_n$ (**2@I$_2$**) (dca = dicyanamide). Herein, the preparation, structural analyses, magnetic, conducting and solid-state electrochemical and spectroelectrochemical properties of the frameworks are studied. Chemical oxidation of the frameworks via iodine doping leads to pronounced variations in these properties, demonstrating the significant potential for redox-modulated multifunctional behavior as the basis of novel molecular electronic and magnetic devices.[6]

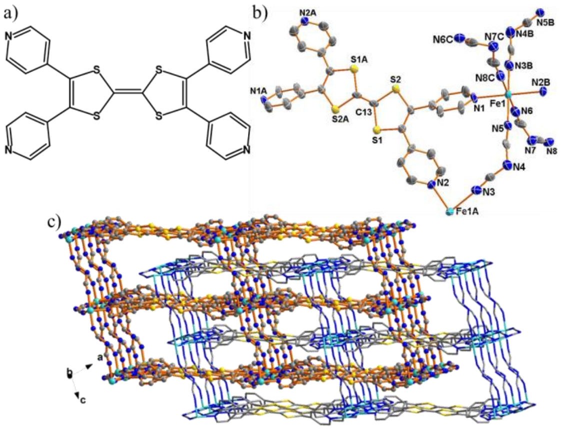

Figure 1. a) The tetra(4-pyridyl)-tetrathiafulvalene (TTF(py)$_4$) ligand; b) Octahedral coordination geometry around the Fe(II) center in **1**; c) View of the 2-fold interpenetrated network in **1**.

The crystal structure of **1** adopts the monoclinic space group $P2_1/c$ and **2** adopts the orthorhombic space group $Pbam$ (Table S1). All the Fe(II) ions are in a distorted [FeN$_6$] octahedral coordination environment. In **1**, the Fe(II) ions are linked by four dca ligands into 2D $[Fe(dca)_2]_n$ layers which are pillared by the TTF(py)$_4$ ligand, thus generating a two-fold interpenetrated 3D framework which can be regarded as a (4,6)-connected binodal sqc173-type topological network (Figure 1, Figure S1, and Table S4). The average Fe−N bond lengths (2.170 Å at 273 K, 2.163 Å

---

[a] H. Y. Wang, Y. Wu, J. Y. Ge, Prof. Dr. J. L. Zuo
State Key Laboratory of Coordination Chemistry
School of Chemistry and Chemical Engineering
Collaborative Innovation Center of Advanced Microstructures,
Nanjing University, Nanjing, 210093 (China)
E-mail: zuojl@nju.edu.cn
[b] C. Hua, C. F. Leong, A/Prof. D. M. D'Alessandro
School of Chemistry, The University of Sydney
Sydney, New South Wales, 2006, Australia
[c] C. Q. Jiao, Prof. Dr.T. Liu
State Key Laboratory of Fine Chemicals
Dalian University of Technology
2 Linggong Rd., 116024 Dalian (China)

Supporting information for this article is given via a link at the end of the document.

at 173 K) for Fe(II) ions exhibit smaller changes, suggesting that these ions are always in the HS state (Table S2).[2b,7] For **2**, four TTF(py)$_4$ ligands act as bridges linking four Fe(II) atoms, generating 2D {Fe[TTF(py)$_4$]}$_n$ undulating layers (Figure S2). These layers are linked by two separate dca species which occupy the axial positions of the Fe(II) ions to form a 3D framework (Figure 2). Thus, the structure can be described as a (4,6)-connected binodal sqc11-type topological network (Table S4). In **2**, the channels contain disordered solvent molecules (two CH_2Cl_2 and four CH_3OH), which was estimated from PLATON (see Supporting Information). The average Fe1−N distance is 2.15 Å at 223 K, suggesting that the Fe1 ions are in HS states. The average Fe1−N distances are 1.97 and 1.96 Å at 173 and 100 K (Table S2), respectively, suggesting the conversion from the HS state to LS state of Fe1 ions.[8] As expected, the unit cell volume decreases upon cooling. The TTF backbone exhibits a Z-like conformation in compound **1** and a U-like conformation in compound **2** (Figure S3). The bond lengths and angles of the TTF(py)$_4$ are close to those reported for the neutral unit (Table S3).[9]

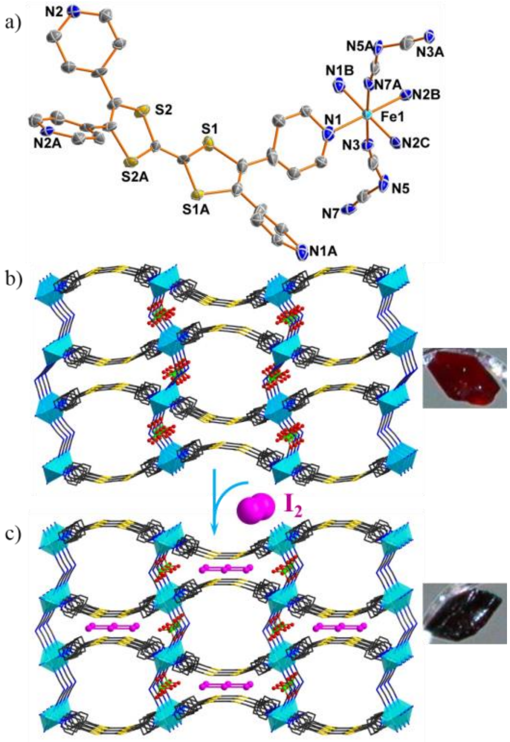

Figure 2. a) Octahedral coordination geometry around the Fe(II) center in **2**; b) View of 3D network of **2** along the *c* axis; c) View of 3D network of **2@I$_2$** along the *b* axis.

Variable-temperature magnetic susceptibilities were measured on polycrystalline samples of **1** and **2** embedded in eicosane at a dc field of 1 kOe (Figure 3a). In the case of **1**, the $\chi_M T$ values remain essentially constant above 50 K with a room temperature value of 3.53 cm^3 mol^{-1} K, which is close to the expected value for the HS Fe(II) ion (S = 2).[10] Below 50 K, the $\chi_M T$ value decreases rapidly and approaches 1.2 cm^3 mol^{-1} K at 2 K; this is attributed to the presence of zero-field splitting of the Fe(II) centers[8] and/or weak antiferromagnetic interactions between the HS-HS ions.[11] For **2**, the $\chi_M T$ value is 3.62 cm^3 mol^{-1} K at 300 K, suggesting a HS Fe(II) ion at ambient temperature.[10] Upon cooling, the $\chi_M T$ value decreases regularly between 175 and 78 K and then reaches a wide plateau of 1.5 cm^3 mol^{-1} K ($T_{1/2}$ = 146 K), which indicates an incomplete SCO transition.[2d] This result from the magnetic data is subtlety different from that for the crystal structure analysis at low temperatures, which may be attributed to the different solvent content of the samples used for single crystal and microanalytical measurments (TGA and elemental analysis data indicate that there is one CH_2Cl_2 and two CH_3OH molecules, Fig. S8 and experimental section). Upon further cooling, the $\chi_M T$ value decreases sharply to 0.70 cm^3 mol^{-1} K at 2 K due to zero-field splitting and/or weak antiferromagnetic interactions of the Fe(II) centers.[12] Thermal hysteresis was not observed in the subsequent warming process.

The ^{57}Fe Mössbauer spectrum of **2** was recorded at 290 and 78 K to characterize the electronic states of the Fe centres and confirm the Fe(II) SCO behavior (Figure S4, Table S5). In the high-temperature phase at 290 K, one quadrupole doublet was observed with Mössbauer parameters of δ (isomer shift) = 0.88 mm s^{-1} and ΔE_Q (quadrupole-split splitting) = 1.12 mm s^{-1} which are characteristic of the HS Fe(II) species.[13] At 78 K, the spectrum consists of two quadruple doublets assigned to the LS Fe(II) (δ = 0.37, ΔE_Q = 0.49 mm s^{-1}) and HS Fe(II) sites (δ = 1.68, ΔE_Q = 2.45 mm s^{-1}); the analysis of the band intensities leads to a A_{HS}/A_{tot} ratio of 39%. The Mössbauer data are consistent with the magnetic measurements and confirm that complex **2** features gradual and incomplete SCO behavior.

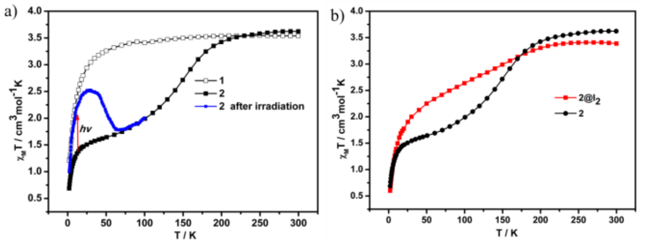

Figure 3. Magnetic properties of a) **1**, **2**, photoexcited **2**, and b) **2** and **2@I$_2$** in the form of $\chi_M T$ versus T.

Photoexcitation measurements on **2** (Figure 3a) indicated the occurrence of the LIESST (light-induced excited spin-state trapping) effect.[13-14] The sample was cooled to 10 K and irradiated with 532 nm laser (P = 30 mW cm^{-2}) for 3.6 h. After reaching photo-excited magnetic saturation, the laser was switched off. Under such treatment, some LS Fe(II) ions were converted to their HS* Fe(II) states.[15] When the sample was heated from 2 K after irradiation, the $\chi_M T$ value increased abruptly and reached its maximum value (2.5 cm^3 mol^{-1} K) at 28 K, which is 69% of the value (3.62 cm^3 mol^{-1} K) measured at 300 K. As the temperature was increased further, the $\chi_M T$ value decreased gradually and reached 1.8 cm^3 mol^{-1} K at 61 K, due to relaxation of the HS* to LS Fe(II) ions.[15] According to the first derivative of the $\chi_M T$ vs. T curves, $T_{(LIESST)}$ was 62 K.[16] These measurements indicate that the magnetization can be increased by light irradiation and recovered via thermal treatment. While a discrete TTF-based complex displaying both SCO and the LIESST effect has been reported,[3f] **2** represents the first example of a TTF-based coordination framework that displays both SCO and the LIESST effect.

Solid-state cyclic voltammetry (CV) of **1** and **2** was performed to investigate the potential for redox modulation of the MOFs (Figures S6). The CV of **1** exhibited two *quasi*-reversible oxidation peaks at 0.28 and 0.56 V in the anodic region, corresponding to the $TTF/TTF^{\bullet +}$ and $TTF^{\bullet +}/TTF^{2+}$ redox couples, respectively. The processes at −2.15 and −2.29 *vs*. Fc/Fc^+ observed in the square wave voltammogram can be assigned to the reduction of the pyridyl rings. The redox processes for **1** are dominated by the redox-active ligand, with the observed peaks corresponding well to the cyclic voltammogram of the ligand in the solution state.[5] The electrochemical properties of **2** can also be predominantly attributed to the redox-active ligand. Two sequential one electron oxidation processes of TTF to its radical cation (0.34 *vs*. Fc/Fc^+) then dication (0.69 *vs*. Fc/Fc^+) are observed in the anodic region. The four reduction processes due to the pyridyl rings in the ligand (−2.17, −2.01, −1.97 and −1.71 *vs*. Fc/Fc^+) were elucidated from the square wave voltammogram.

Given the highly convoluted nature of the CV and square wave voltammetry data, solid state Vis/NIR spectroelectrochemical measurements were conducted to gain insight into the origins of the electrochemical processes for **1** and **2** (Figure 4 and Figures S9 and S10). The spectral data for the chemically oxidized frameworks is supported by *in situ* solid state spectroelectrochemical experiments conducted in $[(n\text{-}C_4H_9)_4N]PF_6/CH_3CN$ electrolyte.[17] Upon increasing the applied potential from 0 to 1.3 V, five new bands appeared at 11500, 15300, 17700, 21600 and 23800 cm^{-1} (Figure 4). The bands at 11500 and 17500 cm^{-1} correspond to formation of the $TTF^{\bullet +}$ radical cation, while the bands at 15300, 21400 and 23700 cm^{-1} may correspond to *d-d* and MLCT transitions of the high spin d^5 Fe(III) formed upon oxidation of the Fe(II) ion. Upon increasing the potential from 1.3 to 1.6 V for **1**, the band at 11300 cm^{-1} due to $TTF^{\bullet +}$ decreases due to formation of the TTF^{2+} dication (Figure S9). The bands are spectrally reversible upon reducing the applied potential to 0 V to regain the starting spectra of the solids (Figures S9 and S10).

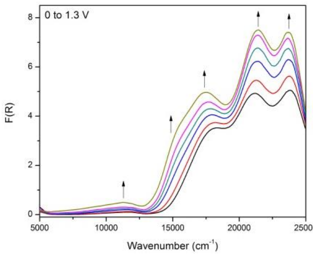

Figure 4. Solid state Vis-NIR spectroelectrochemistry on **1** over the potential range of 0 to 1.3 V.

The solid state UV-Vis-NIR spectra of **1** and **2** exhibit similar characteristics (Figure S7), with high intensity bands at ~18000 and ~38000 cm^{-1} that can be assigned to a combination of $\pi \rightarrow \pi^*$ transitions of the aromatic moieties in the ligand in addition to *d-d* transitions of the HS Fe(II) center. The weak band at ~11500 cm^{-1} is consistent with the radical cation of the TTF moiety, indicating that a small amount of oxidation has occurred in the as-synthesized state.[4b] This band is more intense in **1** than **2**, reflecting the more facile oxidation of the TTF moiety in the former case (from the solid state electrochemical measurements, $TTF/TTF^{\bullet +}$ is at 0.28 *vs*. Fc/Fc^+ in **1** and 0.34 *vs*. Fc/Fc^+ in **2**).

It is well known that the introduction of iodine is an effective synthetic strategy for realizing tunable electrical conductivity in MOFs, and this approach was adopted here in an attempt to realize electronically- and magnetically-tunable functional properties.[18] The I_2-doped **1@I₂** and **2@I₂** were obtained by immersing crystals of **1** and **2** in a solution of iodine in cyclohexane (Figure S11). For the crystal structure of complex **2@I₂**, the asymmetric unit contains one Fe(II) atom, one $TTF(py)_4$ ligand, one ClO_4^- anion, and half a I_3^- anion. The coordination interaction between the $TTF(py)_4$ ligand and the Fe(II) ions leads to a 3D network, which is similar to that of **2** (Figure 2c, Figure S12). Viewing the structure along the *b* axis, two kind of channels are found, in which I_3^- anions are located. The TTF moiety also adopts a U-like configuration (Table S3). The central C=C bond of the TTF units is 1.41(2) Å, which is longer than that of the neutral compound **2**.[19] The results clearly confirm that the TTF moiety is in its radical cation state.[20]

To confirm the oxidation state of iron in the materials, X-ray Photoelectron Spectroscopy (XPS) measurements on **1**, **2**, **1@I₂** and **2@I₂** were carried out (Figure S18). The binding energy position of the main peak is related to the oxidation state of the iron center. Each component consists of two main peaks (711 and 724 eV), which are close to the Fe $2p_{3/2}$ and Fe $2p_{1/2}$ main peaks for Fe(II) (centered at 710.5 and 724 eV, respectively).[21] The values for **1@I₂** and **2@I₂** are consistent with the undoped complexes, supporting the assertion that Fe is completely in the 2+ oxidation state.[22]

An important ramification of redox-state tuning in electroactive MOFs is the potential for modulation of the conducting properties.[6,23] The room temperature electrical conductivities of the I_2-doped **1@I₂** and **2@I₂** are 1.3×10^{-6} and 7.6×10^{-5} S/cm, respectively. These values are 3 orders of magnitude larger than those for **1** (4.1×10^{-9} S/cm) and 2 orders of magnitude larger than those in **2** (1.2×10^{-7} S/cm) at ambient temperature. The altered conductivity can be attributed to a higher content of the TTF radical cation in the doped materials compared to their neutral counterparts. **2@I₂** thus represents a relatively rare example of a redox-active and intrinsically semiconducting coordination polymer that displays SCO.[24] While conductivities for frameworks incorporating the $TTF(py)_4$ ligand have not been reported previously, the semiconducting properties of materials with other TTF-based ligands such as TTFTC (tetrathiafulvalene tetracarboxylate) and TTFTB (tetrathiafulvalene tetrabenzoate) are known, and fall in the semiconducting range of 10^{-4}-10^{-6} S/cm which has been found for the oxidized forms of **1** and **2**.[4f] The mechanisms for charge transport have not been fully elucidated in these systems, however TTF moieties often form π-π stacked columns and short

S···S interactions, which facilitate efficient pathways for charge migration.[4b,25] While it is not possible to speculate about the conduction mechanism in the present case, it is clear that oxidative doping markedly enhances long-range charge transport by increasing the density of free charge carriers.

The corresponding solid state UV-Vis-NIR spectra of the doped samples are shown in Figure S7. Indeed, upon doping **1** and **2** with iodine, the band at ~11500 cm^{-1} intensifies significantly, indicating the formation of an increased amount of the $TTF^{\bullet +}$ radical cation.[18a] Associated with this increase is a red shift of the peak at ~18000 cm^{-1} in the as-synthesized systems to ~17300 cm^{-1} in the oxidized frameworks. To confirm that I_2 was indeed incorporated into the pores of the materials, the doped samples of **1@I$_2$** and **2@I$_2$** were immersed in methanol; the absorbance of I_2 in solution increased with time (Figure S14).[18e,26] Furthermore, diffuse reflectance IR spectra of the frameworks before and after I_2 doping revealed no changes to the cyanide stretching frequencies of the dca ligand (2320, 2245 and 2181 cm^{-1} for **1** and 2332, 2255 and 2185 cm^{-1} for **2** consistent with coordinated dca),[27] which confirms that the dca ligands were not displaced during the iodine treatment (Figure S15). Raman spectroscopy was performed on $TTF(py)_4$, **1**, **1@I$_2$**, **2** and **2@I$_2$** to elucidate the charge of the $TTF(py)_4$ ligand in each material. The peak at 1590 cm^{-1} in the Raman spectrum of $TTF(py)_4$ may be assigned to the C=C ring stretch of the neutral TTF core; this vibrational frequency shifts to lower energies in **1** (1533 cm^{-1}), **1@I$_2$** (1523 cm^{-1}), **2** (1531 cm^{-1}) and **2@I$_2$** (1528 cm^{-1}), concomitant with weakening of the C=C double bond and thus oxidation of the TTF core (Figure S16). XPS anaylsis revealed that the iodine treated samples **1@I$_2$** and **2@I$_2$** contained higher percentages of the TTF radical cation (approximately 1 and 5%, respectively) compared to their neutral counterparts **1** and **2**, respectively, as determined from the ratio of peak integrals of the S 2p band at 164.2 (neutral TTF) and 165.4 eV ($TTF^{\bullet +}$) (Figure S17).[28]

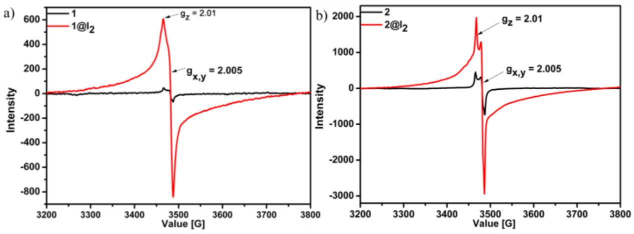

Figure 5. Solid state EPR spectra of a) **1** and **1@I$_2$**, b) **2** and **2@I$_2$** at room temperature.

Electron paramagnetic resonance (EPR) studies of the solid compounds further confirmed the effectiveness of chemical doping (Figure 5). All EPR spectra (which were recorded under the same conditions) showed an axial set of g values ($g_{x,y}$ = 2.005 and g_z = 2.010), typical of $TTF^{\bullet +}$ cation radicals, confirming that the TTF moiety in these compounds is the redox-active unit.[29] A weak signal in the EPR spectrum of pristine **1** and **2** indicates the presence of a very small amount of the TTF moiety in its radical cation form, which is consistent with the weak band at ~11500 cm^{-1} in the UV-Vis-NIR spectra.[30] The EPR signal increased after I_2 doping, clearly validating the increased concentration of the $TTF^{\bullet +}$ radical cation.

A significant aspect of this work was the potential to modulate the magnetic properties of frameworks via redox-state switching. In the case of **2** and **2@I$_2$**, magnetic studies showed that the latter undergoes gradual and incomplete SCO behavior as does its parent framework **2** (Figure 3b), however the shape of the $\chi_M T$ plot changes significantly upon oxidation. The $\chi_M T$ value remained constant at 2.99 $cm^3 mol^{-1} K$ above 200 K. With cooling between 200 and 50 K, the $\chi_M T$ value decreases to 1.97 $cm^3 mol^{-1} K$ with a $T_{1/2}$ value of 128 K. Below 50 K the $\chi_M T$ value decreases rapidly to 0.52 $cm^3 mol^{-1} K$ at 2 K, due to zero field splitting of the Fe(II) centers.[31] The Mössbauer spectrum of **2@I$_2$** was studied at 290 and 78 K (Figure S5 and Table S5). Similarly, for **2@I$_2$** at 290 K, the spectrum consists of one quadrupole doublet assigned to the HS Fe(II) ions (δ = 0.99 mm s^{-1} and ΔE_Q = 1.41 mm s^{-1}). At 78 K, it consists of two quadruple doublets for the LS Fe(II) (δ = 0.37, ΔE_Q = 0.20 mm s^{-1}) and HS Fe(II) (δ = 0.93, ΔE_Q = 3.04 mm s^{-1}) ions and its A_{HS}/A_{tot} ratio is 44%. These data are consistent with the magnetic measurements.

Interestingly, the LIESST effect of sample **2** was absent after doping with I_2 (Figure S19). Given that oxidation of the TTF core to $TTF^{\bullet +}$ affects the ligand field around the Fe(II) center, it is clear that this redox-state modulation is closely related to the magnetic properties.

In conclusion, we demonstrate that two 3D Fe(II) MOFs based on the redox-active tetra(4-pyridyl)-tetrathiafulvalene ligand exhibit multifunctional magnetic, electronic and optical properties of relevance to the development of molecular electronics devices.[32] Complex **2** shows a (4,6)-connected binodal sqc11-type 3D structure, and a crystal-to-crystal structure transformation by I_2 doping has been observed for the first time in this type of material. Solid-state electrochemical studies reveal that the redox activity of the TTF moiety was maintained in both systems, providing a handle to modulate the electrical properties. Compound **2** undergoes an incomplete gradual spin crossover behavior with a LIESST effect at low temperature, representing a rare example of a SCO MOF based on the TTF ligand. Doping iodine into the MOFs not only improves the conductive properties by 2-3 orders of magnitude, but also changes the magnetic properties significantly. These results indicate that **2** is an interesting photo- and electronically-switchable spin crossover material. Importantly, this work demonstrates a unique and highly useful approach for exploiting redox-switchable and multi-stimuli switchable materials. Further investigations on $TTF(py)_4$ compounds with new structures and multifunctional properties are currently underway in our laboratory.

Experimental Section

Synthesis of $\{[Fe(dca)_2][TTF(py)_4]_{0.5}\cdot 0.5CH_2Cl_2\}_n$ (**1**): A solution of $Fe(ClO_4)_2$ (0.02 mmol, 7.24 mg) and Na(dca) (0.04 mmol, 3.54 mg) in CH_3OH (1.5 mL) was stirred for 1 h at room temperature, and was subsequently layered onto a solution of $TTF(py)_4$ (0.02 mmol, 5 mg) in CH_2Cl_2 (1.5 mL). The diffusion was left for 7 days at room temperature, and dark red bar crystals were obtained. Yield, 73% (based on $TTF(py)_4$). Anal. Calcd. for $C_{17.50}H_9ClFeN_8S_2$: C, 43.18; H, 1.86; N, 23.02; S, 13.17.

Found: C, 43.27; H, 1.99; N, 22.85; S, 13.12. Selected IR data (KBr, cm^{-1}): 3417(s), 2360(w), 2310(w), 2175(s), 1603(m), 1540(w), 1418(w), 1219(w), 1090(w), 800(w), 659(w), 630(w).

Synthesis of {[Fe(dca)][TTF(py)$_4$]·ClO$_4$·CH$_2$Cl$_2$·2CH$_3$OH]}$_n$ (**2**): The crystals of **2** were obtained by a similar procedure described for **1**. A solution of Fe(ClO$_4$)$_2$ (0.02 mmol, 7.24 mg) and Na(dca) (0.02 mmol, 1.77 mg) in CH$_3$OH (1.5 mL) was layered onto a solution of TTF(py)$_4$ (0.02 mmol, 5 mg) in CH$_2$Cl$_2$ (1.5 mL). The diffusion was left for 7 days at room temperature, and dark red plate crystals were obtained. Yield, 68% (based on TTF(py)$_4$). Anal. Calcd. for $C_{31}H_{26}Cl_3FeN_7O_6S_4$: C, 42.17; H, 2.97; N, 11.10; S, 14.52. Found: C, 42.05; H, 2.88; N, 11.56; S, 16.98. Selected IR data (KBr, cm^{-1}): 3385(s), 2323(w), 2252(w), 2181(s), 1604(s), 1414(m), 1541(m), 1219(w), 1090(s), 1062(s), 1015(m), 849(w), 799(m), 658(m), 622(m), 540(s).

Acknowledgements

This work was supported by the Major State Basic Research Development Program (No. 2013CB922101), the National Natural Science Foundation of China (No. 91433113 and 91422302), the Natural Science Foundation of Jiangsu Province (No. BK20130054) and the Australian Research Council (No. DP110101671 and DP150100570).

Keywords: multifunctional • Metal-Organic Frameworks • Tetrathiafulvalenes • Switchable • Spin Crossover

[1] a) D. J. Tranchemontagne, J. L. Mendoza-Cortes, M. O'Keeffe, O. M. Yaghi, *Chem. Soc. Rev.*, **2009**, *38*, 1257-1283; b) Y. Sun, L. Sun, D. Feng, H.-C. Zhou, *Angew. Chem., Int. Ed.*, **2016**, *55*, 6471-6475; c) H. C. Zhou, J. R. Long, O. M. Yaghi, *Chem. Rev.*, **2017**, *112*, 673-674.

[2] a) A. Bousseksou, G. Molnar, L. Salmon, W. Nicolazzi, *Chem. Soc. Rev.*, **2011**, *40*, 3313-3335; b) J. J. Amoore, S. M. Neville, B. Moubaraki, S. S. Iremonger, K. S. Murray, J. F. Letard, C. J. Kepert, *Chem. - Eur. J.*, **2010**, *16*, 1973-1982; c) R.-J. Wei, Q. Huo, J. Tao, R.-B. Huang, L.-S. Zheng, *Angew. Chem., Int. Ed.*, **2011**, *50*, 8940-8943; d) R.-J. Wei, J. Tao, R.-B. Huang, L.-S. Zheng, *Eur. J. Inorg. Chem.*, **2013**, *2013*, 916-926; e) Z. Yan, M. Li, H. L. Gao, X. C. Huang, D. Li, *Chem. Commun.*, **2012**, *48*, 3960-3962.

[3] a) T. Mahfoud, G. Molnar, S. Bonhommeau, S. Cobo, L. Salmon, P. Demont, H. Tokoro, S. I. Ohkoshi, K. Boukheddaden, A. Bousseksou, *J. Am. Chem. Soc.*, **2009**, *131*, 15049-15054; b) M. A. Halcrow, *Chem. Soc. Rev.*, **2008**, *37*, 278-289; c) G. J. Halder, C. J. Kepert, B. Moubaraki, K. S. Murray, J. D. Cashion, *Science*, **2002**, *298*, 1762-1765; d) F. J. Munoz-Lara, A. B. Gaspar, M. C. Munoz, V. Ksenofontov, J. A. Real, *Inorg. Chem.*, **2013**, *52*, 3-5; e) M. Nihei, N. Takahashi, H. Nishikawa, H. Oshio, *Dalton Trans.*, **2011**, *40*, 2154-2156; f) F. Pointillart, X. Liu, M. Kepenekian, B. Le Guennic, S. Golhen, V. Dorcet, T. Roisnel, O. Cador, Z. You, J. Hauser, S. Decurtins, L. Ouahab, S. X. Liu, *Dalton Trans.*, **2016**, *45*, 11267-11271; g) J. A. Real, E. Andres, M. C. Munoz, M. Julve, T. Granier, A. Bousseksou, F. Varret, *Science*, **1995**, *268*, 265-267.

[4] a) B. Chen, Z. P. Lv, C. F. Leong, Y. Zhao, D. M. D'Alessandro, J. L. Zuo, *Cryst. Growth Des.*, **2015**, *15*, 1861-1870; b) S. S. Park, E. R. Hontz, L. Sun, C. H. Hendon, A. Walsh, T. Van Voorhis, M. Dinca, *J. Am. Chem. Soc.*, **2015**, *137*, 1774-1777; c) C. F. Leong, B. Chan, T. B. Faust, D. M. D'Alessandro, *Chem. Sci.*, **2014**, *5*, 4724-4728; d) J. L. Segura, N. Martin, *Angew. Chem., Int. Ed.*, **2001**, *40*, 1372-1409; e) C. J. Kepert, D. Hesek, P. D. Beer, M. J. Rosseinsky, *Angew. Chem., Int. Ed.*, **1998**, *37*, 3158-3160; f) H.-Y. Wang, L. Cui, J.-Z. Xie, C. F. Leong, D. M. D'Alessandro, J.-L. Zuo, *Coord. Chem. Rev.*, **2016**, doi:org/10.1016/j.ccr.2016.1010.1011.

[5] a) V. Vajpayee, S. Bivaud, S. Goeb, V. Croué, M. Allain, B. V. Popp, A. Garci, B. Therrien, M. Sallé, *Organometallics*, **2014**, *33*, 1651-1658; b) H. Y. Wang, Y. Wu, C. F. Leong, D. M. D'Alessandro, J. L. Zuo, *Inorg. Chem.*, **2015**, *54*, 10766-10775.

[6] D. M. D'Alessandro, *Chem. Commun.*, **2016**, *52*, 8957-8971.

[7] O. Hietsoi, P. W. Dunk, H. D. Stout, A. Arroyave, K. Kovnir, R. E. Irons, N. Kassenova, R. Erkasov, C. Achim, M. Shatruk, *Inorg. Chem.*, **2014**, *53*, 13070-13077.

[8] W.-T. Liu, J.-Y. Li, Z.-P. Ni, X. Bao, Y.-C. Ou, J.-D. Leng, J.-L. Liu, M.-L. Tong, *Cryst. Growth Des.* , **2012**, *12*, 1482-1488.

[9] R. K. Murmann, C. L. Barnes, *Inorg. Chem.*, **2001**, *40*, 6514-6517.

[10] M. Shatruk, A. Dragulescu-Andrasi, K. E. Chambers, S. A. Stoian, E. L. Bominaar, C. Achim, K. R. Dunbar, *J. Am. Chem. Soc.*, **2007**, *129*, 6104-6116.

[11] S. R. Batten, J. Bjernemose, P. Jensen, B. A. Leita, K. S. Murray, B. Moubaraki, J. P. Smith, H. Toftlund, *Dalton Trans.*, **2004**, 3370-3375.

[12] M. Seredyuk, L. Piñeiro-López, M. C. Muñoz, F. J. Martínez-Casado, G. Molnár, J. A. Rodriguez-Velamazán, A. Bousseksou, J. A. Real, *Inorg. Chem.*, **2015**, *54*, 7424-7432.

[13] T. Liu, H. Zheng, S. Kang, Y. Shiota, S. Hayami, M. Mito, O. Sato, K. Yoshizawa, S. Kanegawa, C. Duan, *Nat. Commun.*, **2013**, *4*, 2826.

[14] a) D.-P. Dong, T. Liu, S. Kanegawa, S. Kang, O. Sato, C. He, C.-Y. Duan, *Angew. Chem., Int. Ed.*, **2012**, *51*, 5016-5016; b) O. Sato, J. Tao, Y.-Z. Zhang, *Angew. Chem., Int. Ed.*, **2007**, *46*, 2152-2187; c) S. Ohkoshi, K. Imoto, Y. Tsunobuchi, S. Takano, H. Tokoro, *Nat. Commun.*, **2011**, *3*, 564-569.

[15] X. Cheng, Q. Yang, C. Gao, B.-W. Wang, T. Shiga, H. Oshio, Z.-M. Wang, S. Gao, *Dalton Trans.*, **2015**, *44*, 11282-11285.

[16] O. Iasco, E. Rivière, R. Guillot, M. Buron-Le Cointe, J.-F. Meunier, A. Bousseksou, M.-L. Boillot, *Inorg. Chem.*, **2015**, *54*, 1791-1799.

[17] P. M. Usov, C. Fabian, D. M. D'Alessandro, *Chem. Commun.*, **2012**, *48*, 3945-3947.

[18] a) S. K. M. Nalluri, N. Shivarova, A. L. Kanibolotsky, M. Zelzer, S. Gupta, P. W. J. M. Frederix, P. J. Skabara, H. Gleskova, R. V. Ulijn, *Langmuir*, **2014**, *30*, 12429-12437; b) C. Wang, D. Zhang, D. Zhu, *J. Am. Chem. Soc.*, **2005**, *127*, 16372-16373; c) Z.-P. Lv, Z.-Z. Luan, H.-Y. Wang, S. Liu, C.-H. Li, D. Wu, J.-L. Zuo, S. Sun, *ACS Nano*, **2015**, *9*, 12205-12213; d) T. Kitamura, S. Nakaso, N. Mizoshita, Y. Tochigi, T. Shimomura, M. Moriyama, K. Ito, T. Kato, *J. Am. Chem. Soc.*, **2005**, *127*, 14769-14775; e) M.-H. Zeng, Z. Yin, Y.-X. Tan, W.-X. Zhang, Y.-P. He, M. Kurmoo, *J. Am. Chem. Soc.*, **2014**, *136*, 4680-4688.

[19] a) E. W. Reinheimer, H. Zhao, K. R. Dunbar, *Synth. Met.*, **2008**, *158*, 447-452; b) S. Yokota, K. Tsujimoto, S. Hayashi, F. Pointillart, L. Ouahab, H. Fujiwara, *Inorg. Chem.*, **2013**, *52*, 6543-6550.

[20] a) F. Setifi, L. Ouahab, S. Golhen, Y. Yoshida, G. Saito, *Inorg. Chem.*, **2003**, *42*, 1791-1793; b) L. Boudiba, A. Gouasmia, S. Golhen, L. Ouahab, *Synth. Met.*, **2011**, *161*, 1800-1804.

[21] L. Castro, R. Dedryvère, M. El Khalifi, P. E. Lippens, J. Bréger, C. Tessier, D. Gonbeau, *J. Phys. Chem. C*, **2010**, *114*, 17995-18000.

[22] a) P. Mills, J. L. Sullivan, *J. Phys. D: Appl. Phys.*, **1983**, *16*, 723-732; b) H. Konno, K. Sasaki, M. Tsunekawa, T. Takamori, R. Furuichi, *Bunseki kagaku*, **1991**, *40*, 609-616.

[23] a) L. Sun, M. G. Campbell, M. Dincă, *Angew. Chem., Int. Ed.*, **2016**, *55*, 3566-3579; b) C. F. Leong, P. M. Usov, D. M. D'Alessandro, *MRS Bull.*, **2016**, *41*, 858-864.

[24] a) W. Xue, B.-Y. Wang, J. Zhu, W.-X. Zhang, Y.-B. Zhang, H.-X. Zhao, X.-M. Chen, *Chem. Commun.*, **2011**, *47*, 10233-10235; b) G. Agustí, R. Ohtani, K. Yoneda, A. B. Gaspar, M. Ohba, J. F. Sánchez-Royo, M. C. Muñoz, S. Kitagawa, J. A. Real, *Angew. Chem., Int. Ed.*, **2009**, *48*, 8944-8947; c) V. Martínez, A. B. Gaspar, M. C. Muñoz, R. Ballesteros, N. Ortega-Villar, V. M. Ugalde-Saldívar, R. Moreno-Esparza, J. A. Real, *Eur. J. Inorg. Chem.*, **2009**, *2009*, 303-310.

[25] a) T. L. A. Nguyen, R. Demir-Cakan, T. Devic, M. Morcrette, T. Ahnfeldt, P. Auban-Senzier, N. Stock, A.-M. Goncalves, Y. Filinchuk, J.-M. Tarascon, G. Férey, *Inorg. Chem.*, **2010**, *49*, 7135-7143; b) T. C. Narayan, T. Miyakai, S. Seki, M. Dincă, *J. Am. Chem. Soc.*, **2012**, *134*, 12932-12935.

[26] a) Z. Yin, Q.-X. Wang, M.-H. Zeng, *J. Am. Chem. Soc.*, **2012**, *134*, 4857-4863; b) M.-H. Zeng, Q.-X. Wang, Y.-X. Tan, S. Hu, H.-X. Zhao, L.-S. Long, M. Kurmoo, *J. Am. Chem. Soc.*, **2010**, *132*, 2561-2563.

[27] L. Tabrizi, H. Chiniforoshan, P. McArdle, *J. Coord. Chem.*, **2015**, *68*, 980-992.

[28] a) D. Choudhury, B. Das, D. D. Sarma, C. N. R. Rao, *Chem. Phys. Lett.*, **2010**, *497*, 66-69; b) C. Bellitto, M. Bonamico, V. Fares, P. Imperatori, S. Patrizio, *J. Chem. Soc., Dalton Trans.*, **1989**, 719-727.

[29] a) R. J. Donohoe, M. Atamian, D. F. Bocian, *J. Am. Chem. Soc.*, **1987**, *109*, 5593-5599; b) Y.-D. Huang, P. Huo, M.-Y. Shao, J.-X. Yin, W.-C. Shen, Q.-Y. Zhu, J. Dai, *Inorg. Chem.*, **2014**, *53*, 3480-3487; c) L. Ćavara, F. Gerson, D. O. Cowan, K. Lerstrup, *Helv. Chim. Acta*, **1986**, *69*, 141-151; d) R. Berridge, P. J. Skabara, C. Pozo-Gonzalo, A. Kanibolotsky, J. Lohr, J. J. W. McDouall, E. J. L. McInnes, J. Wolowska, C. Winder, N. S. Sariciftci, R. W. Harrington, W. Clegg, *J. Phys. Chem. B*, **2006**, *110*, 3140-3152; e) E. Gomar-Nadal, L. Mugica, J. Vidal-Gancedo, J. Casado, J. T. L. Navarrete, J. Veciana, C. Rovira, D. B. Amabilino, *Macromolecules*, **2007**, *40*, 7521-7531.

[30] S.-L. Cai, Y.-B. Zhang, A. B. Pun, B. He, J. Yang, F. M. Toma, I. D. Sharp, O. M. Yaghi, J. Fan, S.-R. Zheng, W.-G. Zhang, Y. Liu, *Chem. Sci.*, **2014**, *5*, 4693-4700.

[31] J. J. M. Amoore, C. J. Kepert, J. D. Cashion, B. Moubaraki, S. M. Neville, K. S. Murray, *Chem. - Eur. J.*, **2006**, *12*, 8220-8227.

[32] a) C. Lefter, V. Davesne, L. Salmon, G. Molnár, P. Demont, A. Rotaru, A.

Bousseksou, *Magnetochemistry*, **2016**, *2*, 18; b) M. M. Khusniyarov, *Chem. - Eur. J.*, **2016**, *22*, 15178-15191.

Entry for the Table of Contents

COMMUNICATION

Two 3D Fe(II) MOFs based on the tetrathiafulvalene-tetrapyridyl ligand and one I_2 doped analogue were fully studied. Complex **1** shows general paramagnetic properties, while complex **2** exhibits gradual and incomplete SCO behavior. The TTF moieties provide redox activity, and I_2 doping can improve their conductive properties. The magnetic properties of **2** could be significantly altered either by doping or light irradiation, indicating that **2** is an interesting electronically- and photo-switchable spin crossover material.

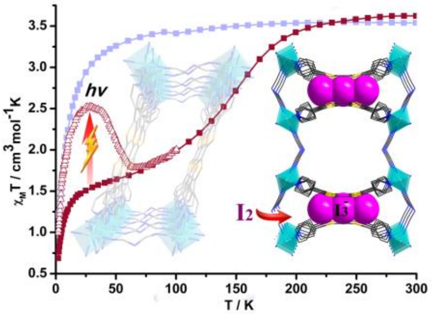

*Hai-Ying Wang, Jing-Yuan Ge, Carol Hua, Cheng-Qi Jiao, Yue Wu, Chanel F. Leong, Deanna M. D'Alessandro, Tao Liu, and Jing-Lin Zuo**

Page No. – Page No.

Photo- and Electronically-Switchable Spin Crossover Iron(II) Metal-Organic Frameworks Based on a Tetrathiafulvalene Ligand

Supporting Information for

Photo- and Electronically-Switchable Spin Crossover Iron(II) Metal-Organic Frameworks Based on a Tetrathiafulvalene Ligand

Hai-Ying Wang,[a] *Jing-Yuan Ge,*[a] *Carol Hua,*[b] *Cheng-Qi Jiao,*[c] *Yue Wu,*[a] *Chanel F. Leong,*[b] *Deanna M. D'Alessandro,*[b] *Tao Liu,*[c] *and Jing-Lin Zuo* *[a]

Contents

Figure S16. Solid state Raman spectroscopy of (a) **1** and **$1@I_2$** and (b) **2** and **$2@I_2$** collected under 785 nm laser excitation.

Figure S17. XPS spectra showing the S 2p region of (a) **1**, (b) **$1@I_2$**, (c) **2** and (d) **$2@I_2$**.

Figure S18. XPS spectra of (a) **1** and**$1@I_2$**; (b) **2** and **$2@I_2$**.

Figure S19. Magnetic properties of **$2@I_2$** and photoexcited **$2@I_2$**

1. Materials and Physical Measurements.

All starting materials were commercially available and were used without further purification. The ligand tetra(4-pyridyl)-tetrathiafulvalene (TTF(py)$_4$) was synthesized according to the literature method.[1]

Thermogravimetric analyses (TGA) were performed using a STA 449C thermal analysis system with a heating rate of 10 °C/min under N_2 conditions. The Bruker D8 Advance X-ray diffractometer equipped with Cu-Kα radiation (λ = 1.5418 Å) was used to collect powder X-ray diffraction (PXRD) data at room temperature. The crystalline powder samples were prepared by crushing the crystals and the PXRD scanned from 5 to 60° at a rate of 5°/min. Calculated PXRD patterns were generated using Mercury 3.0.[2] IR spectra were recorded in range of 400–4000 cm^{-1} on a Vector27 Bruker Spectrophotometer with KBr pellets. C, H, N and S analyses were carried out on a Perkin-Elmer 240C analyzer. Raman spectroscopy was performed on a Renishaw Raman inVia Reflex Spectrometer utilizing a 785 nm excitation laser. Magnetic susceptibility measurements were performed using a Quantum Design SQUID VSM magnetometer on micro crystalline samples for all compounds. Zero-field ^{57}Fe Mössbauer spectra were separately recorded on a Topologic 500A spectrometer at 77.8 K with a proportional counter. ^{57}Co(Rh) moving in a constant acceleration mode was used as the radioactive source. The temperature of the sample was controlled by a Model 9700 digital temperature controller from Scientific Instruments company. Liquid nitrogen is continuously transferred through a high efficiency superinsulated line to a copper sample mount inside the cryostat vacuum jacket. The Doppler velocity of the spectrometer was calibrated with respect to α-Fe. All spectra were fitted to Lorentzian profiles by the least-squares method, and the fit quality was controlled by the standard χ^2 and misfit tests (MossWinn program). In this way, the ^{57}Fe Mössbauer spectral parameters could be determined, including the isomer shift (IS), the electric quadrupole splitting (ΔE_Q), the full width at half maximum, and the relative resonance areas of the different components of the absorption patterns. The sample was encapsulated in a sample holder to avoid loss of solvent molecules when pulling a vacuum on the cryostat. EPR spectra were obtained by using a Bruker EMX-10/12 variable-temperature apparatus.

Solid state cyclic voltammetry measurements were performed in n-Bu_4NPF_6/CH_3CN electrolyte using a BASi Epsilon electrochemical analyser and three electrode system. Argon was bubbled through solutions of 0.1 M $[(n\text{-}C_4H_9)_4N]PF_6$ dissolved in distilled CH_3CN. The CVs were recorded using a glassy carbon working electrode (1.5 mm diameter), a platinum wire auxiliary electrode and an Ag/Ag$^+$ wire *quasi*-reference electrode. The sample was mounted on the glassy carbon working electrode by dipping the electrode into a paste made of the powder sample in CH_3CN. Ferrocene was added as an internal standard upon completion of each experiment. All potentials are reported in mV versus Fc/Fc$^+$ couple.

Solid-state UV/Vis/NIR spectra were obtained on the samples at room temperature using a CARY5000 Spectrophotometer equipped with a Harrick Praying Mantis accessory over the wavenumber range 5000-40000 cm^{-1}. $BaSO_4$ was used for the baseline. Spectra are reported as the Kubelka-Munk transform, where $F(R) = (1-R)^2/2R$ (R is the diffuse reflectance of the sample as compared to $BaSO_4$). Solution-state UV-vis spectra were measured on a UV-3100 spectrophotometer.

Solid-state diffuse reflectance Vis/NIR spectroelectrochemistry was obtained *in situ* in a 0.1 M $[(n\text{-}C_4H_9)_4N]PF_6/CH_3CN$ electrolyte over the range 5000-25000 cm^{-1} using a Harrick Omni

Diff Probe attachment and a custom built solid-state spectroelectrochemical cell.[3] The cell consisted of a Pt wire counter electrode and a Ag/Ag^+ *quasi*-reference electrode. The solid sample was immobilized onto a 0.1 mm thick Indium-Tin-Oxide (ITO) coated glass slide (which acted as the working electrode) using a thin strip of Teflon tape. The applied potential was controlled using an eDAQ potentiostat.

The conductivity of the samples were obtained from Keithley 2400 source meter at room temperature. The sample powders were cold-pressed under pressure of 10 Mpa into pellets, which were connected to the source meter by a gold wire via the conductive carbon adhesive. The conductivity σ could be expressed as, $\sigma = L / (R \times S)$, where L and R are the thickness, resistance of the pellet, respectively, and S is the area of the conductive carbon adhesive.

For the photomagnetic measurements, a powdered sample of **2**, which was spread on a commercial transparent adhesive tape, was used to study the photo-effects. The weight of the sample on the tape was determined by measuring the weight of the tape before and after spreading the sample and determining the difference. The photoirradiation of the samples was performed at 10 K with a laser diode pumped Nd:YAG laser (λ = 532 nm, 30 mW/cm^2, 3.6 h). The temperature-dependent magnetization was measured both before and after irradiation in the temperature range from 2 to 100 K. The difference in the magnetization before and after irradiation was extracted by subtracting the magnetization value before irradiation from that after irradiation. Furthermore, from these magnetization values and the sample weight, the differences in the χT values before and after irradiation ($\Delta\chi T$) were calculated.

2. Synthesis of 1@I_2 and 2@I_2.

The iodine doping of **1@I_2** and **2@I_2** was undertaken using a diffusion technique. Crystals of **2** were soaked in a solution of iodine in cyclohexane (0.05 M) at room temperature for 2 days (Figure S11).[4] Note that the color of the crystals became deeper as the doping time was increased. The crystals obtained were washed with cyclohexane. The quantities of iodine incorporated were confirmed by thermogravimetric analysis (TGA) (Figure S8) and elemental analysis (EA): 0.65 I_2 for **1** per unit cell. Anal. Calcd. for **1@I_2**: C, 32.25; H, 1.39; N, 17.19; S, 9.84. Found: C, 31.96; H, 1.55; N, 17.23; S, 10.07. Selected IR data (KBr, cm^{-1}): 3404(w), 2311(w), 2243(w), 2176(s), 1602(m), 1417(w), 1217(w), 1064(w), 800(w), 659(m), 631(w), 511(w). Anal. Calcd. for **2@I_2** $\{[Fe(dca)][TTF(py)_4]\cdot 0.5I_3\cdot ClO_4\cdot CH_2Cl_2\cdot CH_3OH\cdot C_6H_{12}]\}_n$: C, 38.42; H, 3.05; N, 8.71; S, 11.39. Found: C, 38.62; H, 3.33; N, 8.68; S, 11.25. Selected IR data (KBr, cm^{-1}): 3402(m), 2180(s), 1602(s), 1497(m), 1415(m), 1215(w), 1091(s), 844(w), 791(w), 657(w), 622(m), 536(w).

To ensure that the bulk materials were truly representative of the crystal structures, powder X-ray diffraction (PXRD) experiments for **1**, **2**, **1@I_2**, and **2@I_2** were carried out at room temperature (Figure S13).

3. Single crystal X-ray Crystallography

The crystal statistics were collected with Cu Kα radiation (λ = 1.54178 Å) on a CCD diffractometer. The cell parameters were retrieved and refined by using computer software (SMART and SAINT, respectively).[5] The SADABS[6] program was applied for absorption corrections. Structures were solved by direct methods using the program package SHELXL-97.[7] All the non-hydrogen atoms were located in the Fourier maps and refined with anisotropic parameters. Some contribution of the electron density in compound of **2** from the remaining solvent molecules was removed by the SQUEEZE routine in PLATON.[8] The total void volume of the channels excluding guest molecules, calculated by PLATON, is about 36% for **2** at 100 K.[9] Two CH_2Cl_2 and four CH_3OH per formula unit calculated based upon electron count analysis were removed by SQUEEZE.[10] Crystallographic data in CIF format have been deposited in the Cambridge Crystallographic Data Centre (CCDC) under deposition numbers 1481986–1481990 and 1520728. Crystal data are summarized in Table 1. The framework and the guest solvent molecules for **2** were extremely disordered and seriously unstable; thus, better crystallographic data at 223 K could not be obtained.

Table S1. Crystal data of **1**, **2** and **2@I$_2$**.

	1	
T(K)	173	273
empirical formula	$FeC_{17.50}H_9N_8S_2Cl$	$FeC_{17.50}H_9N_8S_2Cl$
M_r	486.75	486.75
wavelength (Å)	1.54184	1.54184
crystal system	Monoclinic	Monoclinic
space group	$P2_1/c$	$P2_1/c$
a (Å)	8.2936(4)	8.3755(5)
b (Å)	16.2539(9)	16.2549(10)
c (Å)	17.0073(11)	17.0748(13)
V (Å$^{3)}$	2257.7(2)	2280.6(3)
Z	4	4
Crystal size (mm)	0.23×0.12×0.09	0.23×0.12×0.09
P_{calcd} (g cm^{-3})	1.432	1.418
M (mm^{-1})	8.353	8.269
reflns collected	7936	7933
unique reflns	3988(0.0720)	3948(0.0827)
S	1.025	0.995
R_1[a], wR_2[b] ($I > 2\sigma(I)$)	0.0857, 0.2213	0.0954, 0.2445

		2		**2@I$_2$**
T(K)	100	173	223	190
empirical formula	$FeC_{28}H_{16}N_7O_4S_4Cl$	$FeC_{28}H_{16}N_7O_4S_4Cl$	$FeC_{28}H_{16}N_7O_4S_4Cl$	$FeC_{28}H_{16}N_7O_4S_4ClI_{1.50}$
M_r	734.02	734.02	734.02	924.37
wavelength (Å)	1.54184	1.54184	1.54184	1.54184
crystal system	Orthorhombic	Orthorhombic	Orthorhombic	Orthorhombic
space group	*P*bam	*P*bam	*P*bam	Pmna
a (Å)	29.9290(19)	29.846(2)	15.348(3)	29.956(2)
b (Å)	15.4982(12)	15.6718(17)	30.693(2)	9.7331(7)
c (Å)	9.6833(7)	9.6937(10)	9.8227(8)	15.5271(12)
V (Å$^{3)}$	4491.6(6)	4534.1(8)	4627.3(9)	4527.2(6)
Z	4	4	4	4
Crystal size (mm)	0.27×0.16×0.03	0.27×0.16×0.03	0.27×0.16×0.03	0.13 x 0.09 x 0.02
P_{calcd} (g cm^{-3})	1.085	1.075	1.054	1.356
M (mm^{-1})	5.261	5.212	5.107	13.264
reflns collected	10911	11204	10359	10095
unique reflns	4278(0.1101)	4313(0.1081)	4327(0.1291)	4102(0.0471)
S	1.055	1.060	0.967	1.088
R_1[a], wR_2[b] ($I > 2\sigma(I)$)	0.1216, 0.3077	0.1196, 0.3101	0.1316, 0.3373	0.1105, 0.3174

[a]$R_1 = \Sigma||Fo| - |Fc||/\Sigma|Fo|$; [b]$wR_2 = [\Sigma w(F_o^2 - F_c^2)^2/\Sigma w(F_o^2)^2]^{1/2}$.

Table S2. Fe−N Bond Lengths <Fe−N> (Å) around the Fe Sites in the Crystal Structure of **1** and **2** at Different Temperatures

Compound **1**			Compound **2**			
	173 K [a]	273 K [a]		100 K[a]	173 K [a]	223 K [a]
Fe(1)-N(1)	2.195(5)	2.214(5)	Fe(1)-N(1)	2.000(7)	2.000(7)	2.193(7)
Fe(1)-N(2)#3	2.212(5)	2.218(5)	Fe(1)-N(2)#4	1.980(6)	1.987(6)	2.155(15)
Fe(1)-N(3)#3	2.149(6)	2.151(7)	Fe(1)-N(3)	1.928(10)	1.943(8)	2.113(16)
Fe(1)-N(5)	2.163(5)	2.166(6)	Fe(1)-N(7)#2	1.935(10)	1.957(9)	2.054(14)
Fe(1)-N(6)	2.123(7)	2.129(8)				
Fe(1)-N(8)#2	2.135(7)	2.141(8)				
[a]Data derived from single crystal X-ray diffraction analyses.						

Table S3. Summary of Important Structural Parameters for the TTF(4-py)$_4$ ligand of complexes **1** and **2**.

complex	T(K)	conformation	central C=C bond distance (Å)	dihedral angle for TTF core (deg)
1	173	Z	1.329(12)	4.099
	273		1.329(13)	5.252
2	100	U	1.390(13)	18.24, 18.11
	173		1.355(13)	18.68, 18.59
	223		1.294(16)	14.54, 22.52
2@I$_2$	190K	U	1.41(2)	15.87

Table S4. The result of “TOPOS 4.0 professional”.

```
#################
```

1: $FeC_{17.50}H_9N_8S_2Cl$

```
#################
Topology for Sc1
--------------------
Common vertex with                                      R(A-A)
Fe 1       1.4880       0.2448       0.7727     ( 2 1 1)        9.557A            1
Fe 1     -0.4880     -0.2448       0.2273     (-1-1 0)        9.557A            1
Fe 1       1.5120     -0.2552       0.7273     ( 1 0 0)        9.581A            1
Fe 1     -0.5120       0.2552       0.2727     ( 0-1 0)        9.581A            1
Topology for Fe1
--------------------
Atom Fe1 links by bridge ligands and has
Common vertex with                                      R(A-A)
```

```
Fe 1      0.4880      1.2552      0.2727     ( 1 0 0)       8.151A            1
Fe 1      0.4880      0.2552      0.2727     ( 1-1 0)       8.151A            1
Fe 1      0.5120      0.7448      0.7273     ( 0 1 0)       8.547A            1
Fe 1      0.5120      0.7448     -0.2727     ( 0 1-1)       8.547A            1
Sc 1      1.5000      1.0000      0.5000     ( 1 1 0)       9.557A            1
Sc 1     -0.5000      0.5000      0.0000     ( 0 0 0)       9.581A            1
-------------------------
Structural group analysis
-------------------------
-------------------------
Structural group No 1
-------------------------
Structure consists of 3D framework with Fe2Sc
There are 2 interpenetrating nets
FIV: Full interpenetration vectors
----------------------------------
[1,0,0] (8.45A)
----------------------------------
PIC: [2,0,0][0,1,0][0,0,1] (PICVR=2)
Zt=2; Zn=1
Class Ia    Z=2
Coordination sequences
----------------------
Sc1:    1    2    3     4     5     6     7     8      9     10
Num      4 16 38    76 102 178 194 324    314    514
Cum      5 21 59 135 237 415 609 933 1247 1761
----------------------
Fe1:    1    2    3     4     5     6     7     8      9     10
Num      6 18 44    72 116 162 224 288    368    450
Cum      7 25 69 141 257 419 643 931 1299 1749
----------------------
TD10=1753
Vertex symbols for selected sublattice
--------------------------------------
Sc1 Point (Schlafli) symbol:{3^2;6^2;7^2}
Extended point symbol:[3.3.6(3).6(3).7(10).7(10)]
--------------------------------------
Fe1 Point (Schlafli) symbol:{3^2;4^4;5^4;6^4;7}
Extended point symbol:[3.3.4.4.4.4.5.5.5.5.6.6.6(2).6(2).7(2)]
--------------------------------------
Point (Schlafli) symbol for net: {3^2;4^4;5^4;6^4;7}2{3^2;6^2;7^2}
4,6-c net with stoichiometry (4-c)(6-c)2; 2-nodal net
Topological type: sqc173 {3^2;4^4;5^4;6^4;7}2{3^2;6^2;7^2} - VS [3.3.4.4.4.4.6.6.6.6.6.6.*.*.*]
[3.3.6(3).6(3).*.*]    (66909 types in 9 databases)
```

```
Please contact the EPINET database for details: http://epinet.anu.edu.au/sqc173
Elapsed time: 17.19 sec.

########################
```

2: $FeC_{28}H_{16}N_7O_4S_4Cl$

```
########################
Topology for Sc1
Atom Sc1 links by bridge ligands and has
Common vertex with                                  R(A-A)
Fe 1     0.2890     1.2334     0.0110    ( 0 1 0)     8.942A      1
Fe 1     0.2110     0.7334     0.9890    ( 0 0 1)     8.992A      1
Fe 1     0.2890     1.2334     1.0110    ( 0 1 1)     9.036A      1
Fe 1     0.2110     0.7334    -0.0110    ( 0 0 0)     9.125A      1
Topology for Fe1
--------------------
Atom Fe1 links by bridge ligands and has
Common vertex with                                  R(A-A)
Fe 1     0.7890     0.2666    -0.0110    ( 0 0 0)     7.828A      1
Fe 1    -0.2110     0.2666    -0.0110    (-1 0 0)     7.828A      1
Sc 1     0.3377    -0.0189     0.5019    ( 0-1 0)     8.942A      1
Sc 1     0.1623     0.4811     0.4981    ( 0-1 1)     8.992A      1
Sc 1     0.3377    -0.0189    -0.4981    ( 0-1-1)     9.036A      1
Sc 1     0.1623     0.4811    -0.5019    ( 0-1 0)     9.125A      1
-------------------------
Structural group analysis
-------------------------
-------------------------
Structural group No 1
-------------------------
Structure consists of 3D framework with FeSc
Coordination sequences
----------------------
Sc1   1   2   3    4    5    6    7    8     9    10
Num     4 16 38   66 102 146 198 258   326   402
Cum     5 21 59 125 227 373 571 829 1155 1557
----------------------
Fe1   1   2   3    4    5    6    7    8     9    10
Num     6 18 38   66 102 146 198 258   326   402
Cum     7 25 63 129 231 377 575 833 1159 1561
----------------------
TD10=1559
Vertex symbols for selected sublattice
--------------------------------------
Sc1 Point (Schlafli) symbol{4^4;6^2}
```

```
Extended point symbol[4.4.4.4.6(4).6(4)]
--------------------------------------
Fe1 Point (Schlafli) symbol{4^4;6^10;8}
Extended point symbol[4.4.4.4.6(2).6(2).6(5).6(5).6(5).6(5).6(5).6(5).6(5).6(5).8(20)]
--------------------------------------
Point (Schlafli) symbol for net {4^4;6^10;8}{4^4;6^2}
4,6-c net with stoichiometry (4-c)(6-c); 2-nodal net
Topological type fsc; sqc11 {4^4;6^10;8}{4^4;6^2} - VS [4.4.4.4.6(2).6(2)]
[4.4.4.4.6(5).6(5).6(5).6(5).6(5).6(5).6(5).6(5)...]    (66909 types in 9 databases)
Elapsed time 5.93 sec.
```

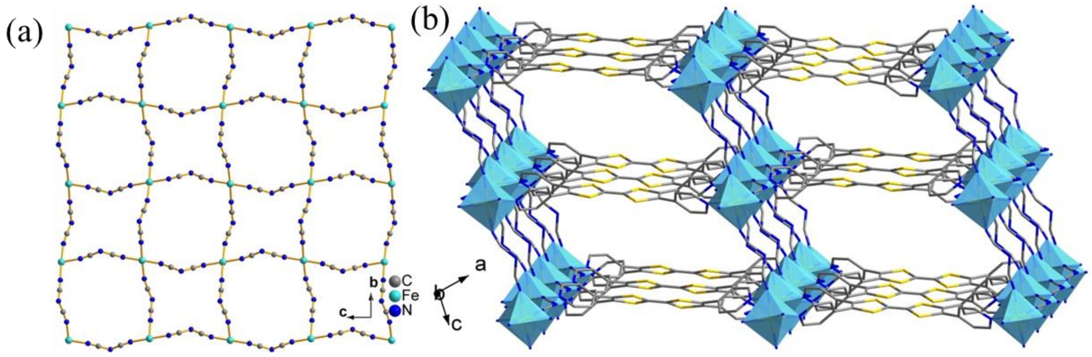

Figure S1. (a) $[Fe(dca)_2]_n$ 2D network. (b) the 3D network (viewed down the *c* axis)

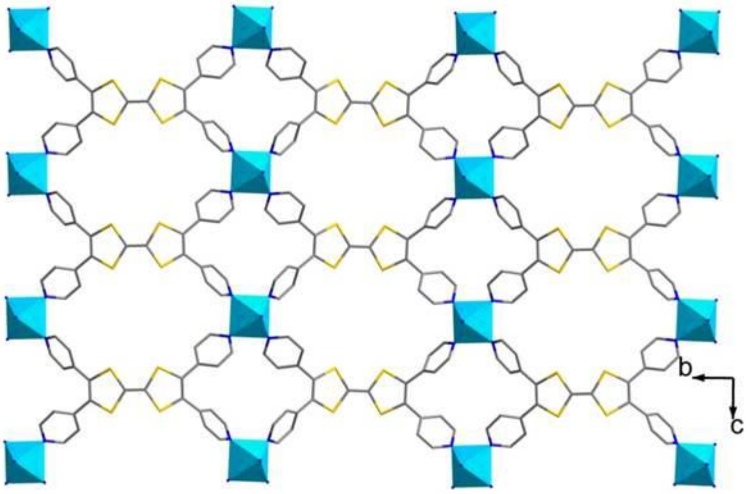

Figure S2. $\{Fe[TTF(py)_4]\}_n$ 2D network.

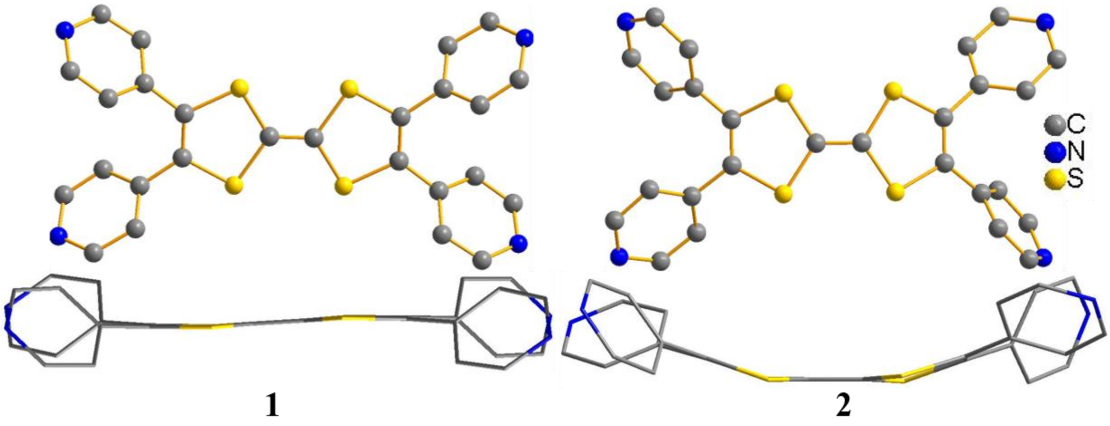

Figure S3. Conformations of the $TTF(py)_4$ ligand in compounds **1** and **2**. Hydrogen atoms have been removed for clarity.

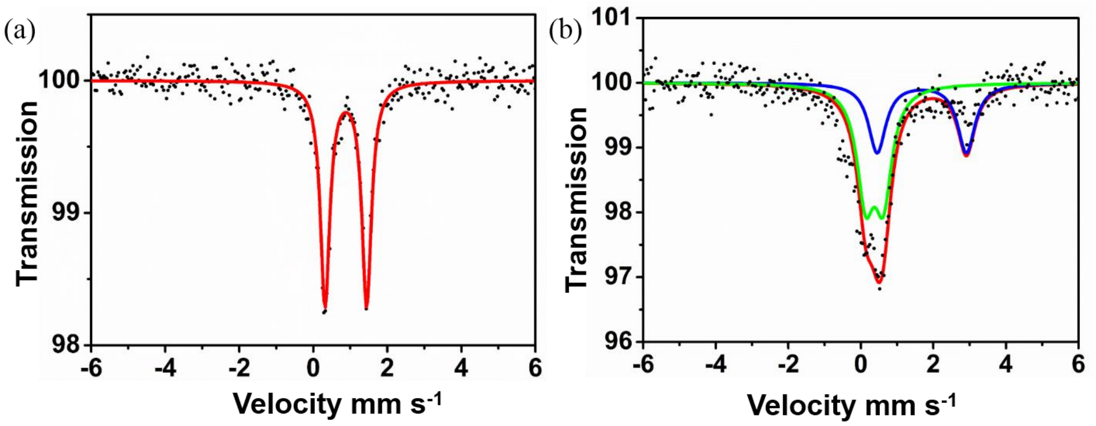

Figure S4. Mössbauer spectra of **2** at (a) 290 and (b) 78 K.

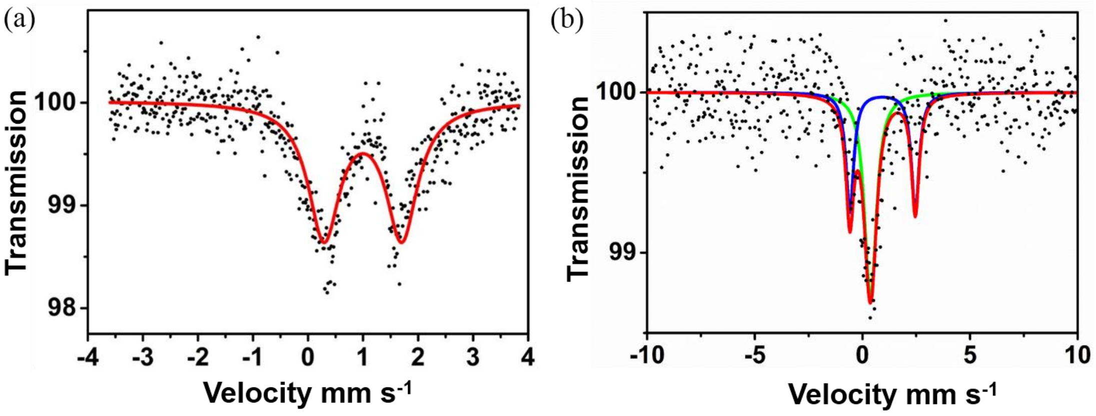

Figure S5. Mössbauer spectra of **2@I$_2$** at (a) 290 and (b) 78 K.

Table S5. Mössbauer Spectra Parameters for **2** and **2@I$_2$**

T (K)	δ (mm s^{-1})	ΔE_Q (mm s^{-1})	Γ (mm s^{-1})	A_{HS}/A_{tot} (%)
2				
290	0.88(1)	1.12(1)	0.31(1)	100
78	1.68(1)	2.45(1)	0.58(1)	39
	0.37(1)	0.49(1)	0.58(1)	
2@I$_2$				
290	0.99(1)	1.41(1)	0.69(1)	100
78	0.93(1)	3.04(1)	0.43(1)	44
	0.37(1)	0.20(1)	0.58(1)	

δ, isomer shift; ΔE_Q, quadrupole-split splitting; Γ, line width; A_{HS}/A_{tot}, area ratio.

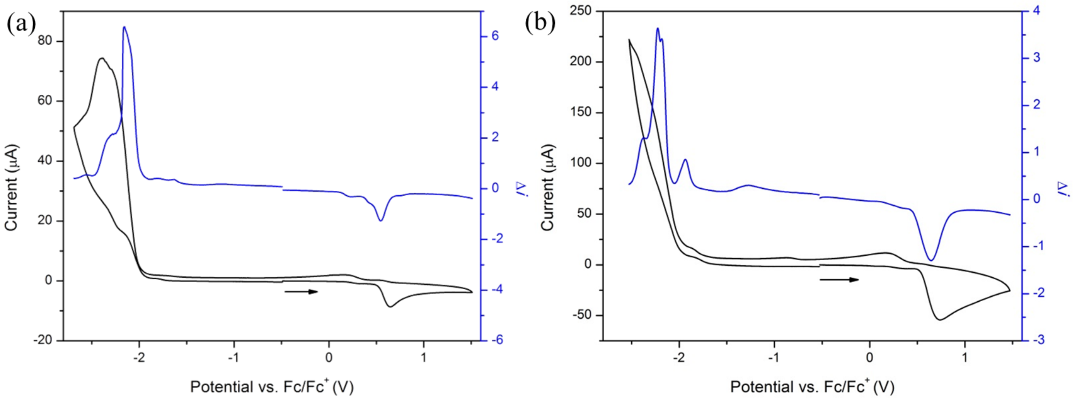

Figure S6. Solid-state cyclic voltammograms of (a) **1** and (b) **2** collected at 100 mV/s square wave voltammogram recorded with an amplitude of 10 mV and frequency of 9 Hz in $[(n\text{-}C_4H_9)_4N]PF_6/CH_3CN$ electrolyte. Arrow indicates the direction of the forward scan.

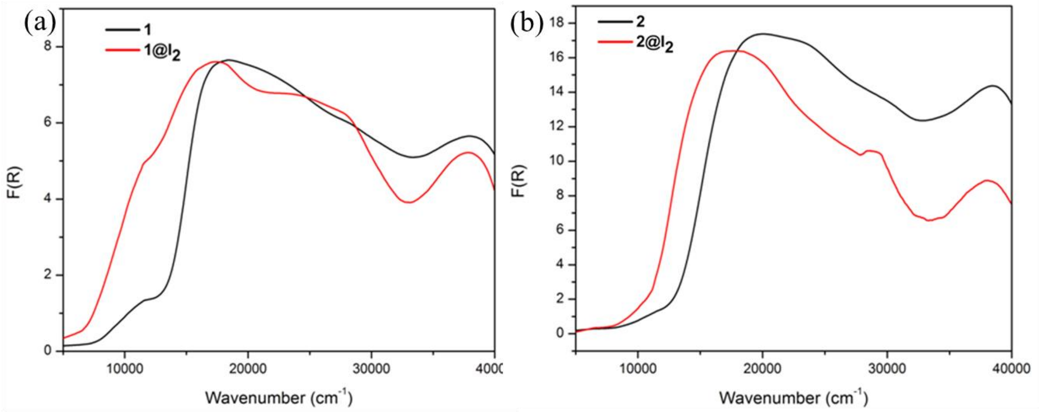

Figure S7. Solid-state UV-Vis-NIR for (a) **1** and **1@I$_2$**, (b) **2** and **2@I$_2$**.

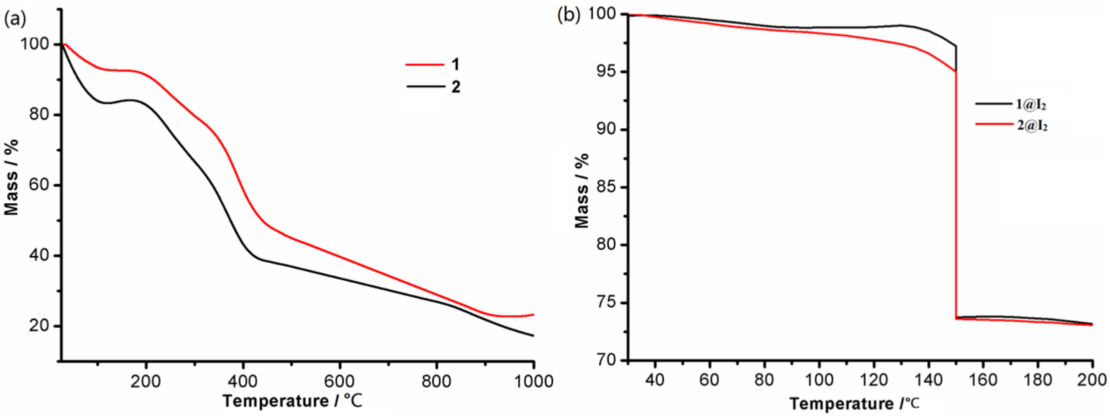

Figure S8. TG plots for (a) **1** and **2**; (b) **1@I$_2$** and **2@I$_2$** at a rate of 5 °C per minute and a pause of 120 minutes at 150 °C.

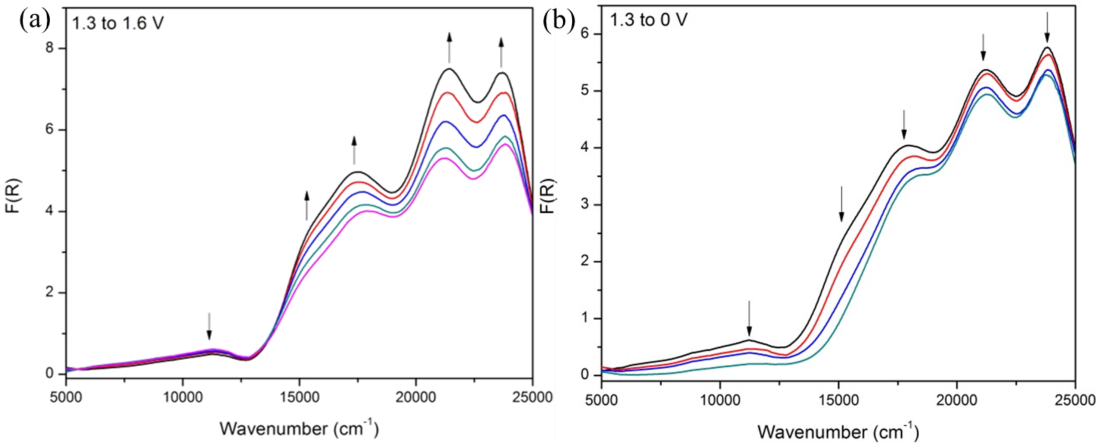

Figure S9. Solid state Vis-NIR spectroelectrochemistry on **1** where (a) 1.3 to 1.6 V, (b) 1.3 to 0 V.

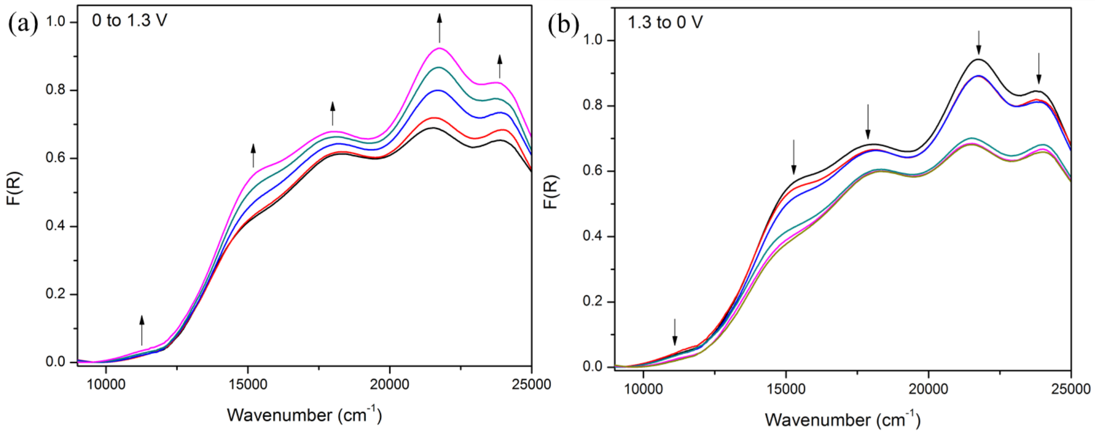

Figure S10. Solid state Vis-NIR spectroelectrochemistry on **2** where (a) 0 to 1.3 V, (b) 1.3 to 0 V.

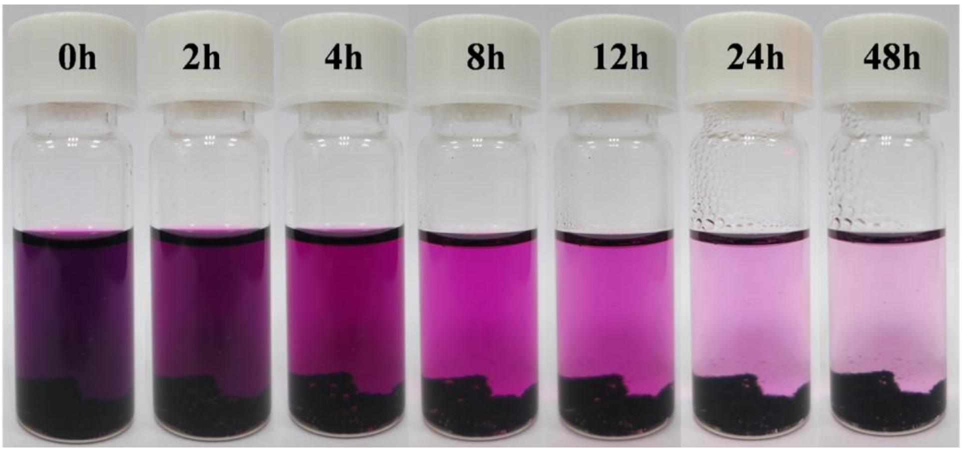

Figure S11. I_2 doping progress when 20 mg of crystals of **2** were soaked in 3 mL solution of iodine in cyclohexane (0.05 M) at room temperature.

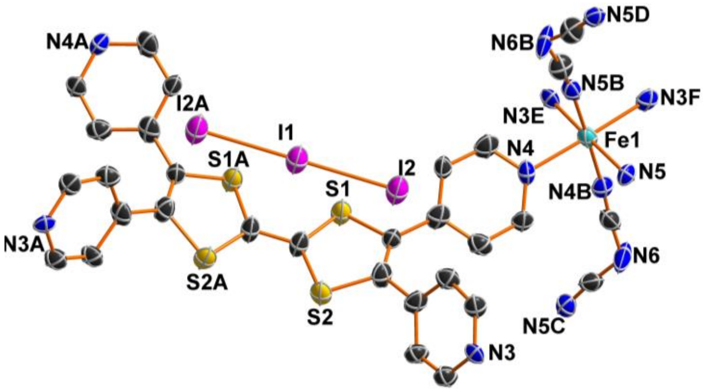

Figure S12. Octahedral coordination geometry around the Fe(II) center in **2@I$_2$**.

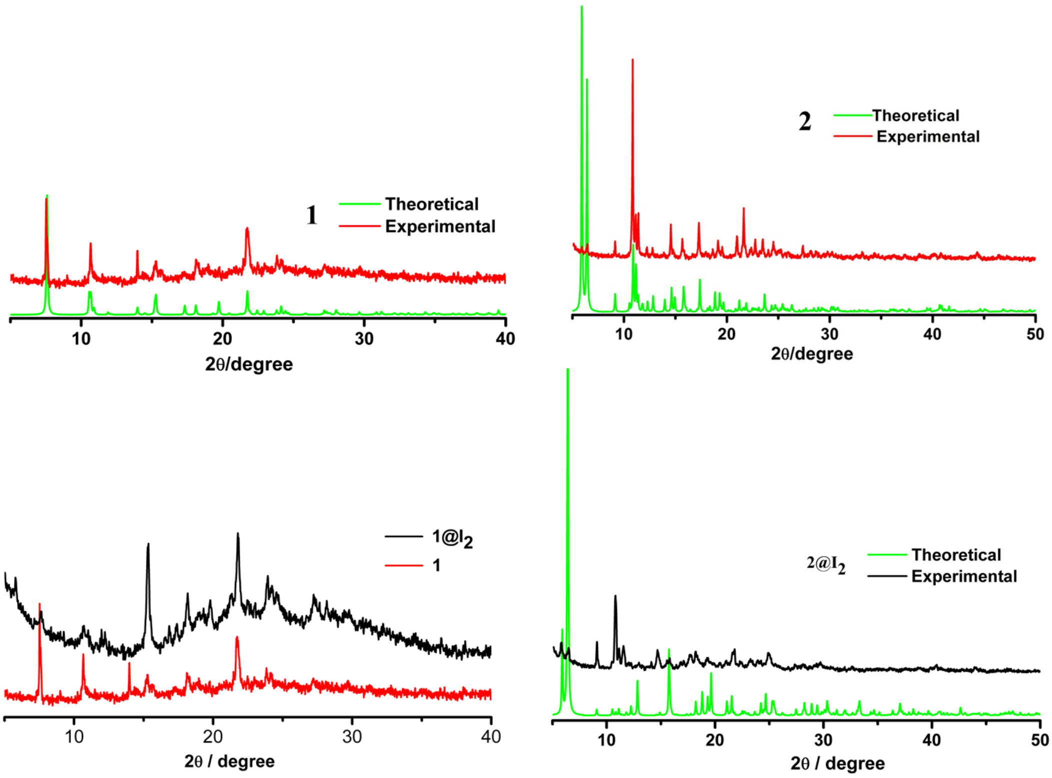

Figure S13. Powder X-ray diffraction (PXRD) patterns of compounds **1**, **1@I$_2$**, and **2**, **2@I$_2$**.

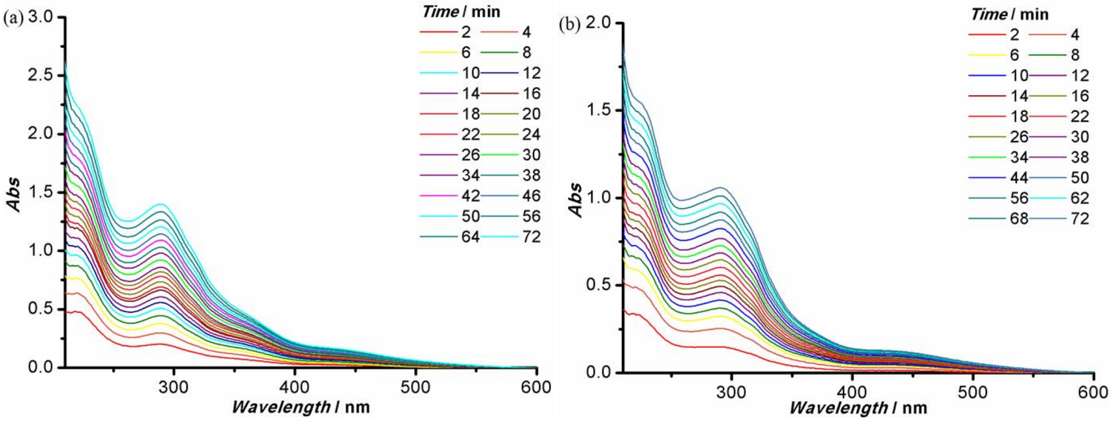

Figure S14. Temporal evolution of UV/vis absorption spectra for the I$_2$ release of (a) **1@I$_2$** and (b) **2@I$_2$** in methanol.

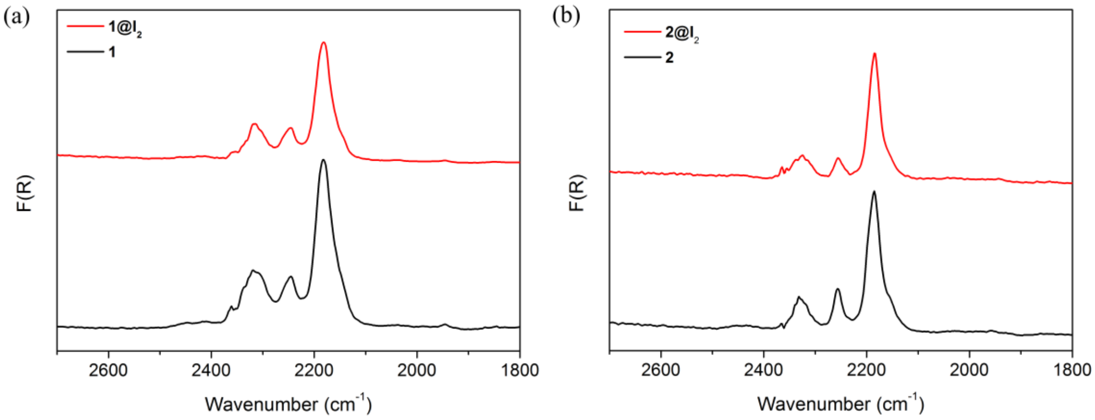

Figure S15. Diffuse reflectance IR spectra of (a) **1** and **1@I$_2$** and (b) **2** and **2@I$_2$** showing the cyanide stretching region.

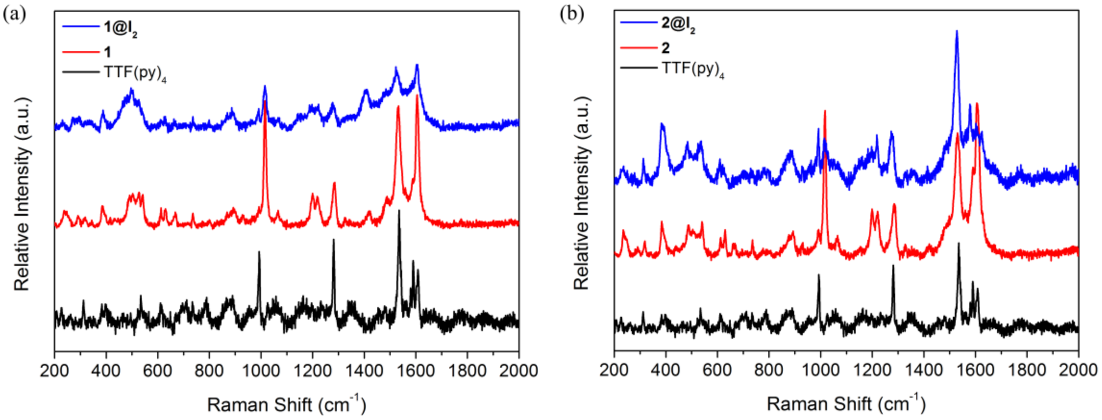

Figure S16. Solid state Raman spectroscopy of (a) **1** and **1@I$_2$** and (b) **2** and **2@I$_2$** collected under 785 nm laser excitation.

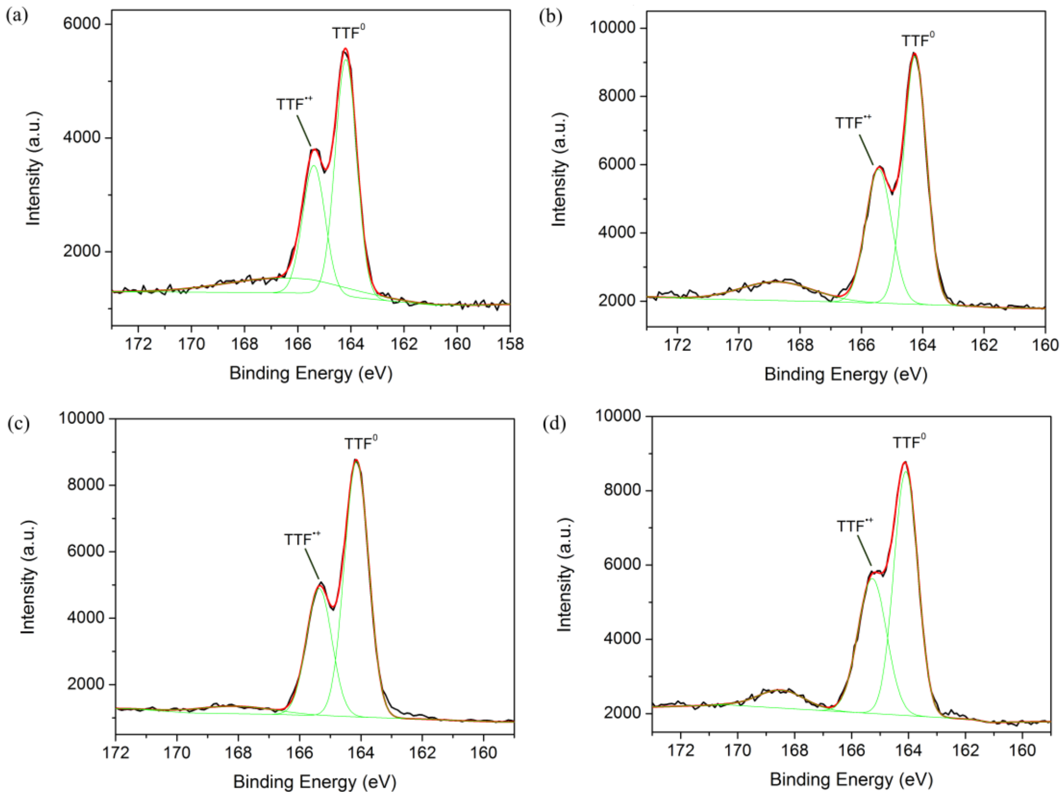

Figure S17. XPS spectra showing the S 2p region of (a) **1**, (b) **1@I$_2$**, (c) **2** and (d) **2@I$_2$**.

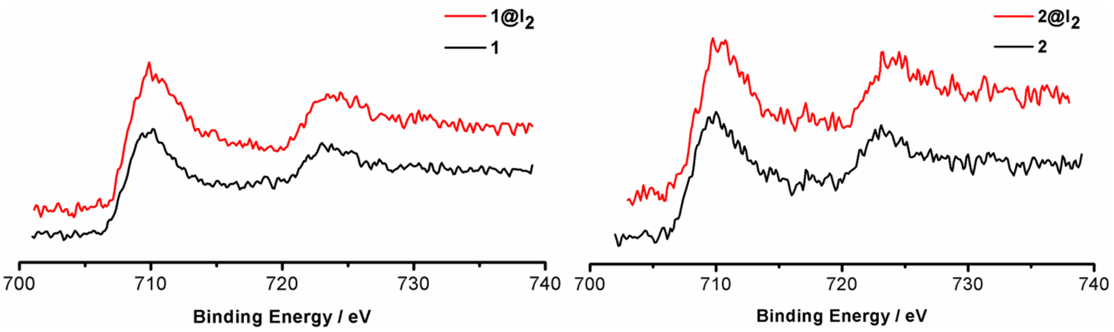

Figure S18. XPS spectra of (a) **1** and**1@I$_2$**; (b) **2** and **2@I$_2$**.

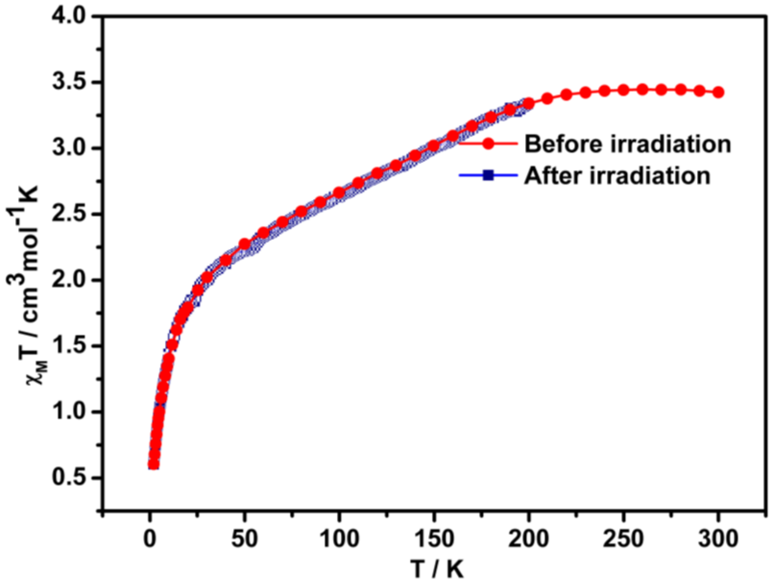

Figure S19. Magnetic properties of **2@I$_2$** and photoexcited **2@I$_2$**

References:

1. Vajpayee, V.; Bivaud, S.; Goeb, S.; Croué, V.; Allain, M.; Popp, B. V.; Garci, A.; Therrien, B.; Sallé, M., *Organometallics* **2014**, *33*, 1651-1658.

2. a) Murdock, C. R.; McNutt, N. W.; Keffer, D. J.; Jenkins, D. M., *J. Am. Chem. Soc.* **2014**, *136*, 671-678; b) Iremonger, S. S.; Liang, J.; Vaidhyanathan, R.; Shimizu, G. K. H., *Chem. Commun.* **2011**, *47*, 4430-4432.

3. Usov, P. M.; Fabian, C.; D'Alessandro, D. M., *Chem. Commun.* **2012**, *48*, 3945-3947.

4. Yu, F.; Li, D.-D.; Cheng, L.; Yin, Z.; Zeng, M.-H.; Kurmoo, M., *Inorg. Chem.* **2015**, *54*, 1655-1660.

5. *SAINT-Plus, version 6.02*; Bruker Analytical X-ray Systems: Madison, WI, 1999.

6. Sheldrick, G. M. SADABS: *An Empirical Absorption Correction Program*; Bruker Analytical X-ray Systems: Madison, WI, 1996.

7. Sheldrick, G. M. *Acta Crystallogr., Sect. A: Found. Crystallogr*. **2008**, *A64*, 112−122.

8. Platon program: Spek, A. L. *Acta Crystallogr., Sect. A* **1990**, *46*, 194−201.

9. A. L. Spek, in *PLATON*, A Multipurpose Crystallographic Tool; Utrecht University: Utrecht, The Netherlands, **2003**.

10. Bi, Y.; Wang, X.-T.; Liao, W.; Wang, X.; Wang, X.; Zhang, H.; Gao, S., *J. Am. Chem. Soc.* **2009**, *131*, 11650-11651.